JAMES | Journal of Advances in Modeling Earth Systems

RESEARCH ARTICLE
10.1029/2020MS002384

Inherent Dissipation of Upwind-Biased Potential Temperature Advection and its Feedback on Model Dynamics

A. Gassmann[1]

[1]Leibniz-Institute of Atmospheric Physics e.V. at the Rostock University (IAP), Kühlungsborn, Germany

Key Points:

- The local antidiffusion within upwind potential temperature advection schemes leads to negative dissipation
- This antidiffusion induces spurious accelerations in the wind field in one-dimensional and full model runs
- Entropically consistent schemes are less accurate and exhibit higher amplitudes of front-generated gravity waves

Correspondence to:
A. Gassmann,
gassmann@iap-kborn.de

Citation:
Gassmann, A. (2021). Inherent dissipation of upwind-biased potential temperature advection and its feedback on model dynamics. *Journal of Advances in Modeling Earth Systems*, *13*, e2020MS002384. https://doi.org/10.1029/2020MS002384

Received 23 OCT 2020
Accepted 22 FEB 2021

Abstract Higher order upwind-biased advection schemes are often used for potential temperature advection in dynamical cores of atmospheric models. The inherent diffusive and antidiffusive fluxes are interpreted here as the effect of irreversible sub-gridscale dynamics. For those, total energy conservation and positive internal entropy production must be guaranteed. As a consequence of energy conservation, the pressure gradient term should be formulated in Exner pressure form. The presence of local antidiffusive fluxes in potential temperature advection schemes foils the validity of the second law of thermodynamics. Due to this failure, a spurious wind acceleration into the wrong direction is locally induced via the pressure gradient term. When correcting the advection scheme to be more entropically consistent, the spurious acceleration is avoided, but two side effects come to the fore: (i) the overall accuracy of the advection scheme decreases and (ii) the now purely diffusive fluxes become more discontinuous compared to the original ones, which leads to more sudden body forces in the momentum equation. Therefore, the amplitudes of excited gravity waves from jets and fronts increase compared to the original formulation with inherent local antidiffusive fluxes. The means used for supporting the argumentation line are theoretical arguments concerning total energy conservation and internal entropy production, pure advection tests, one-dimensional advection-dynamics interaction tests and evaluation of runs with a global atmospheric dry dynamical core.

Plain Language Summary For ease of calculation, an alternative to using the internal energy equation is to consider the movement of an air parcel which maintains a constant value related to temperature and pressure (potential temperature). The pressure gradient converts the energy from internal to kinetic or vice versa, thereby influencing the direction and speed of wind. Hence, in the total energy conservation law, the pressure gradient force and the potential temperature transport equation are interdependent. Equations that simulate the movement the air parcels and its properties (advection equations) have been developed to provide accurate and consistent results. This article reviews whether contemporary advection methods for potential temperature are consistent. This means ensuring the underlying physical laws are met, in particular, the second law of thermodynamics, stating that field variables need to be diffused. However, most numerical advection methods can occasionally act in an antidiffusive way. The pressure inherits this antidiffusion from the potential temperature, if the density is held constant. Due to antidiffusion, the modeled wind direction may be incorrect. Avoiding antidiffusion prevents this effect, but leads to sudden pressure forces. These forces lead to higher gravity wave crests generated at the fronts of weather systems.

1. Introduction

Numerical transport schemes for scalars are often inherently diffusive, because they are formulated as upwind advection schemes or as flux limiter schemes. The textbook of Durran (2010) provides an excellent overview of such schemes. The advantage of these very accurate transport schemes is that they are very selective in their inherent diffusion or antidiffusion properties. Therefore, they suppress the most obvious negative property of centered finite difference schemes, namely the small scale ripples evolving due to the dependence of the dispersion error on the represented wavelengths.

The most prominent scalar in the dynamical core of an atmospheric model is the thermodynamic variable. Many atmospheric models transport the potential temperature in their dynamical cores, other models

transport temperature. It is argued here, that the specific numerical advection properties have some feedback onto the full dynamics. This aspect is not considered in the usual idealized tests for tracer advection schemes. However, this should be done, because the very selective inherent diffusion/antidiffusion mechanisms for thermodynamic variables might feedback onto the formation of perturbations in the wind field. These become the more important for research the more one is interested in the interpretation of simulated smaller scale processes like the formation of gravity waves near jets, fronts and convective clouds (O'Sullivan & Dunkerton, 1995; Plougonven & Zhang, 2014; Schoon & Zülicke, 2018). Namely, the diffusion/antidiffusion of temperature has an effect onto the pressure field if the density is not likewise diffused, as it is standard philosophy. Because of the equation of state, the diffusive/antidiffusive tendencies of temperature are proportionally inherited to the pressure. The pressure gradient may accelerate the wind into different directions depending on the diffusion/antidiffusion property. This might modify the formation of gravity waves.

The other question, which is usually not posed in the context of the advection schemes, is whether the inherent diffusion/antidiffusion mechanisms are in coherence with underlying laws of thermodynamics. For instance, energy conservation and internal entropy production could be taken as accompanying theoretical constraints for modeling (Bannon, 2002; Catry et al., 2007; Degrauwe et al., 2016; Eldred & Gay-Balmaz, 2020; Gassmann & Herzog, 2008, 2015). So far, such constraints are merely consulted for the formulation of the continuous form of scalar advection. It has to be discussed, which consequences such kinds of constraints have for the discrete formulation of a numerical model.

The present contribution wants to discuss both mentioned aspects for the case of potential temperature advection. The tools to attack these points are theoretical considerations of thermodynamic laws (Section 2), inspection of inherent diffusion properties of stand-alone advection schemes (Section 3), a simplified one-dimensional study of advection-dynamics interaction (Section 4), and the judgment of different advection schemes within the dynamical core of the ICON-IAP model (Gassmann, 2013, 2018) in Section 5. Then, the focus will be on the excitation of gravity waves from fronts. Conclusions are given in Section 6.

2. Theoretical Considerations of Hydro-Thermodynamic Laws

Fluid dynamic equations can be disentangled into two parts. One part represents the reversible dynamics and another part represents the irreversible terms. The reversible system can be cast into the form of Hamiltonian dynamics (Dubos & Tort, 2014; Gassmann & Herzog, 2008; Névir & Sommer, 2009). The irreversible part must contribute to energy dissipation (Gassmann & Herzog, 2015). Alternatively expressed, internal entropy production is positive, then.

A very simplified one-dimensional subsystem containing only sound waves and advection reads for the reversible part

$$\partial_t \varrho = -\partial_x(\varrho u) \tag{1}$$

$$\partial_t u = -\partial_x \frac{u^2}{2} - \frac{1}{\varrho}\partial_x p = -\partial_x \frac{u^2}{2} - c_p \theta \partial_x \Pi \tag{2}$$

$$\partial_t(c_v \varrho T) = c_p \Pi \partial_t(\varrho\theta) = -\partial_x(c_v \varrho u T) - p\partial_x u = -c_p \Pi \partial_x(\varrho u \theta). \tag{3}$$

As usual, the involved measures here are ϱ, the density, p, the pressure, and T, the temperature. The specific heat capacities at constant pressure and volume are c_p and c_v, respectively. The horizontal wind component is denoted by u. We note that the pressure gradient term can be represented in two ways, either using the density and the pressure or using the potential temperature $\theta = T/\Pi$ and the Exner pressure $\Pi = (p \,/\, p_{ref})^{R/c_p}$. The thermodynamic equation can either be expressed by the internal energy transport term and the work term or by joining those terms into one term, which represents the adiabatic motion. This can be easily represented as $d_t\theta = 0$.

It is obvious that total energy as a sum of kinetic and internal energy is conserved for the given reversible system in a periodic domain or a closed domain with zero fluxes at the boundaries. This fact is found by noting several product rules of differentiation

$$\frac{u^2}{2}\partial_t\varrho + \varrho u\partial_t u + \partial_t(c_v\varrho T) = -\frac{u^2}{2}\partial_x(\varrho u) - \varrho u\partial_x\frac{u^2}{2} - u\partial_x p - p\partial_x u - \partial_x(c_v\varrho uT) \tag{4}$$

$$= -\frac{u^2}{2}\partial_x(\varrho u) - \varrho u\partial_x\frac{u^2}{2} - \varrho u c_p\theta\partial_x\Pi - c_p\Pi\partial_x(\varrho u\theta) \tag{5}$$

$$\partial_t\left(\varrho\left(c_vT + \frac{u^2}{2}\right)\right) = -\partial_x\left(\varrho u\frac{u^2}{2} + c_p\varrho uT\right). \tag{6}$$

Note that the last line is independent of the actual pressure gradient formulations employed in Equations 4 and 5, because $c_p\varrho T = c_p\varrho\theta\Pi = p + c_v\varrho T$.

Now, when adding subgrid-scale or diffusive terms to this equation set, then the Navier-Stokes equation just adds the friction term and the internal energy equation allows for an irreversible heat flux divergence and has to account for frictional heating

$$\partial_t u\,|_{sub,1} = -\frac{1}{\varrho}\partial_x(-\varrho K^D\partial_x u) \tag{7}$$

$$\partial_t(c_v\varrho T)\,|_{sub,1} = -\partial_x(-c_p\varrho K^T\partial_x T) + \varrho K^D(\partial_x u)^2 \tag{8}$$

$$\partial_t\varrho\,|_{sub,1} = 0. \tag{9}$$

here, the diffusion and volume viscosity coefficients are K^T and K^D, respectively. Note that the continuity equation is not equipped with a subgrid-scale term (In the context of turbulence averaging, this notion leads to the preference of mass-weighted (Hesselberg or Favre) averages over non-mass-weighted Reynolds averages). The additional terms reflect also energy conservation in the previously mentioned domain, as can be seen by multiplying the wind tendency with ϱu and adding the result to the thermodynamic tendency

$$\partial_t\left(\varrho\left(c_vT + \frac{u^2}{2}\right)\right)|_{sub,1} = -\partial_x\left(-c_p\varrho K^T\partial_x T - \varrho K^D\partial_x\frac{u^2}{2}\right). \tag{10}$$

The Gibbs fundamental relation, documented, for example, in de Groot and Mazur (1984), expresses internal energy changes in terms of work $\delta\tilde{W}$ and heat changes $\delta\tilde{Q}$. It reads for our problem

$$c_v\varrho\, d_tT = \underbrace{-p\partial_x u}_{\delta\tilde{W}} + \underbrace{T\varrho\, d_t s}_{\delta\tilde{Q}} \tag{11}$$

where s is the specific thermodynamic entropy and d_t expresses the individual derivative (If optionally changes in air compositions are counted as well by adding the term $\sum_i\mu_i\varrho d_tq_i$—where the specific contents are q_i and the chemical potentials are μ_i—this term is counted as a work term and not as a heat term). From this, a prognostic entropy equation is found by inserting the full internal energy equation, that is the sum of Equations 6 and 8 and dividing by T. This gives

$$\varrho\, d_t s = -\frac{\partial_x(-c_p\varrho K^T\partial_x T)}{T} + \frac{\varrho K^D(\partial_x u)^2}{T}. \tag{12}$$

Now, the second law of thermodynamics is a statement about the internal entropy production. Therefore, entropy fluxes over boundaries have to be disentangled from an eventual local production of entropy. Then, the entropy budget equation becomes

$$\varrho d_t s = -\partial_x \left(\frac{-c_p \varrho K^T \partial_x T}{T} \right) + \frac{c_p \varrho K_T (\partial_x T)^2}{T^2} + \frac{\varrho K^D (\partial_x u)^2}{T}. \tag{13}$$

Each of the last two internal entropy production terms, $\sigma_T = (c_p \varrho K^T (\partial_x T)^2) / T^2$ and $\sigma_{fr} = \varrho K^D (\partial_x u)^2 / T$, is positive definite if the diffusion and volume viscosity coefficients are positive. The total energy dissipation ε due to irreversible heat fluxes and friction is related to the internal entropy production by $\varepsilon_T = T\sigma_T$ and $\varepsilon_{fr} = T\sigma_{fr}$, hence $\varepsilon = \varepsilon_T + \varepsilon_{fr}$. Frictional dissipation means that kinetic energy is irreversibly converted into internal energy. Thermal dissipation means that a part of the internal energy is made unavailable by temperature diffusion. It is important to stress that the term "energy dissipation" is *not always* associated with energy conversions between different energy compartments, rather it expresses how much energy is made *un*available for further reversible processes. This is the classic thermodynamic viewpoint (de Groot & Mazur, 1984).

In meteorological thinking, the potential temperature has an outstanding character. Motions in a dry atmosphere are essentially adiabatic. Therefore, the potential temperature is a favorable prognostic variable to be transported by a numerical scheme. Often, this is accomplished by inherently diffusive numerical schemes (Durran, 2010). This inherent diffusion or subscale contribution can be extracted into own contributions for the prognostic equations. The associated tendencies read then

$$\partial_t u \mid_{sub,2} = c_p \frac{K^\theta \partial_x \theta}{u} \partial_x \Pi \tag{14}$$

$$\partial_t (c_v \varrho T) \mid_{sub,2} = c_p \Pi \partial_t (\varrho\theta) \mid_{sub,2} = -c_p \Pi \partial_x (-\varrho K^\theta \partial_x \theta) \tag{15}$$

$$\partial_t \varrho \mid_{sub,2} = 0. \tag{16}$$

The index 2 indicates that these subscale terms differ from those of the classical viewpoint given above. The new subgrid-scale terms guarantee also energy conservation, because

$$\partial_t \left(\varrho \left(c_v T + \frac{u^2}{2} \right) \right) \mid_{sub,2} = \partial_x (c_p \varrho K^\theta \Pi \partial_x \theta). \tag{17}$$

Obviously, the unexpected additional subgrid-scale pressure gradient term is required to accomplish this energetic consistency. Likewise, a meaningful entropy budget equation is to be found

$$\varrho d_t s = -\partial_x \left(-\frac{c_p \varrho K^\theta \partial_x \theta}{\theta} \right) + \frac{c_p \varrho K^\theta (\partial_x \theta)^2}{\theta^2} \tag{18}$$

with an entropy production term $\sigma_\theta = (c_p \varrho K^\theta (\partial_x \theta)^2) / \theta^2$, which delivers positive energy dissipation $\varepsilon = T\sigma_\theta$ for positive diffusion coefficients.

Both approaches for subgrid-scale terms have their pros and cons. The version 1 is unambiguously founded on classical thermodynamics, and therefore unquestionable. But, if applying it to nearly adiabatic flow in which the potential temperature remains nearly constant for an air parcel, or said in other words, the dynamics is driven by the advection of potential temperature nearly alone, then it is unclear whether version 1 can accomplish this when considering that the work term and the temperature advection term are independently discretized. In this sense, version 2 is much more attractive. Adding a slight inherent diffusion to the quasi-tracer θ is common practice in numerical modeling. The interplay between internal energy transport and adiabatic expansion or compression remains then stuck together also for subgrid-scale dynamics that arises due to inherent diffusion of advection schemes. And intuitively, this is immediately plausible. We want to call this behavior quasi-adiabatic.

But, version 2 is not without problems. The problem is that u appears in the denominator of Equation 14, and so the diffusion coefficient K^θ must be formulated such that it prevents division by zero. This insight also says that the diffusion coefficient K^θ must depend on the dynamical state of the system, namely

u itself. It is impossible that this coefficient becomes a constant even for arbitrarily small scales of motion. Therefore, this mechanism loses its dominating role when the numerical resolution reaches viscous and molecular scales. At those scales, the subgrid-scale terms of version 1 are unambiguously right and have to be used with constant material coefficients. Direct Numerical Simulations (DNS) must thus work with the subgrid-scale formulation 1. Version 2 is thus only an option for Large Eddy Simulations (LES) and coarser grained models. A numerical model designed for a wide range of regimes could thus contain both formulations for subgrid-scale terms. The scales of motion where this model is applied determine then which of the two formulations dominates the relative magnitudes of subgrid-scale tendencies. Such regime transitions may occur within one model domain. For instance, models reaching up to the thermosphere encounter the turbopause, in which turbulent mixing ceases compared to the viscous and molecular terms. A model containing subgrid-scale types 1 and 2 would thus be perfectly suited for such deep atmospheric modeling.

3. Numerical Advection Schemes Reconsidered

3.1. Characteristics of Advection Schemes

We note that for quasi-adiabatic flow, the potential temperature equation is just represented by the advection equation. On a C-staggered mesh, numerical advection schemes are written in flux form

$$\partial_t(\varrho\theta)_i = -\frac{1}{\Delta x}(U_{i+1/2}\hat{\theta}_{i+1/2} - U_{i-1/2}\hat{\theta}_{i-1/2}) \tag{19}$$

with the mass flux $U_{i+1/2} = u_{i+1/2}(\varrho_i + \varrho_{i+1})/2$. Such schemes differ in the numerical approximation to the edge value $\hat{\theta}_{i+1/2}$. For our purpose, we must first disentangle the purely advective part of the flux from the nonadvective part of this flux. The diffusion coefficient has then to be diagnosed from the nonadvective part. Hence, for every flux we can write

$$U_{i+1/2}\hat{\theta}_{i+1/2} = U_{i+1/2}\left(\overline{\theta}_{i+1/2} - \frac{K^{\theta}_{i+1/2}\delta_x\theta_{i+1/2}}{u_{i+1/2}\Delta x}\right) \tag{20}$$

where $\overline{\theta}_{i+1/2} = (\theta_{i+1} + \theta_i)\,/\,2$ and $\delta_x\theta_{i+1/2} = \theta_{i+1} - \theta_i$. Here, we want to call the first term on the right the advective part of the flux and the second term on the right the non-advective part. The simple centered average $\overline{\theta}_{i+1/2}$ for the advective part can be motivated by the fact that the Exner pressure gradient term in Equation 2 awaits such a centered averaging for its prefactor θ, because relations $\theta\partial_x\Pi = \partial_x(\Pi\theta) - \Pi\partial_x\theta$ should also be numerically recovered.

The numerical expression for a flux in flux limiting schemes is often given in the form

$$\text{for } U_{i+1/2} \geq 0: \qquad F_{i+1/2} = U_{i+1/2}\left(\theta_i + \frac{C(r)}{2}(1 - \mu_{i+1/2})(\theta_{i+1} - \theta_i)\right) \tag{21}$$

$$\text{for } U_{i+1/2} < 0: \qquad F_{i+1/2} = U_{i+1/2}\left(\theta_{i+1} + \frac{C(r)}{2}(1 - \mu_{i+1/2})(\theta_i - \theta_{i+1})\right), \tag{22}$$

where μ is the local Courant number (Durran, 2010, Chapter 5). The flux depends on a specific function $C(r)$, and r is the slope ratio

$$\text{for } U_{i+1/2} \geq 0: \qquad r = \frac{\theta_i - \theta_{i-1}}{\theta_{i+1} - \theta_i} \tag{23}$$

$$\text{for } U_{i+1/2} < 0: \qquad r = \frac{\theta_{i+2} - \theta_{i+1}}{\theta_{i+1} - \theta_i}. \tag{24}$$

For the goal to separate the diffusion coefficient out, we want to disentangle the time discretization aspect from the space discretication aspect. Since the $\mu_{i+1/2}$ in the factor $1 - \mu_{i+1/2}$ accounts for a second order

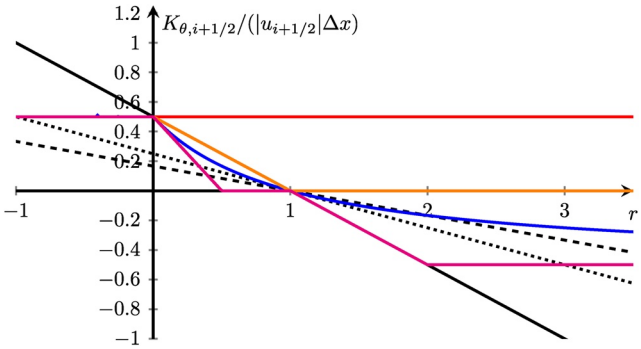

Figure 1. Diagnosed nondimensional diffusion coefficient for different methods as a function of r. Red: First order upwind. Black solid: Beam Warming. Black dashed: Third order upwind. Black dotted: Fromm. Blue: van Leer limiter. Orange: Minmod limiter. Magenta: Superbee limiter.

in time aspect, but not for a spatial discretization aspect, it is omitted here. Instead, the so defined new fluxes might be applied within common Runge Kutta time integration schemes. It is clear, that also the time integration itself contributes to inherent damping of a solution, if the amplification factor of the scheme is smaller than 1. This aspect is not discussed here, but could be worthwhile to be inspected in later work.

The such defined fluxes can likewise be cast in the above given form Equation 20, which distinguishes diffusion aspects from advection aspects. The diffusion coefficient can be read off and it gives

$$K^{\theta}_{i+1/2} = \mid u_{i+1/2} \mid \Delta x \frac{1 - C(r)}{2}. \tag{25}$$

here, the diffusion coefficient depends linearly on $|u_{i+1/2}|$. Therefore, the potential singularity discussed for the pressure gradient term in Equation 14 is prevented automatically by such schemes. The u-terms in the enumerator and denominator cancel out. Typical known schemes and the associated diffusion coefficients are listed here

$$\begin{aligned}
\text{A) No diffusion:} C(r) &= 1,\\
\text{B) Constant diffusion:} &\text{n. a.},\\
\text{C) First order upwind:} C(r) &= 0,\\
\text{D) Beam Warming:} C(r) &= r,\\
\text{E) Fromm:} C(r) &= \frac{1+r}{2},\\
\text{F) 3rd order upwind:} C(r) &= \frac{2+r}{3},\\
\text{G) van Leer:} C(r) &= \frac{r+\mid r \mid}{1+\mid r \mid},\\
\text{H) Minmod:} C(r) &= \max(0,\min(1,r)),\\
\text{I) Superbee:} C(r) &= \max(0,\min(1,2r),\min(2,r)),
\end{aligned}$$

The constant diffusion scheme is not part of the given context, because it does not prevent the singularity in Equation 14. It can only be applied to the diffusion of the temperature itself when subgrid-scale type 1 applies. The first order upwind scheme is diffusive, and the diffusion does not further depend on the flow structure of the θ-field. The diffusion coefficients of the Beam Warming scheme, the Fromm scheme and the third order scheme have the same shape but become smaller the higher the order of the scheme, which is indicated by different factors in the denominators

$$K^{\theta}_{i+1/2} = u_{i+\frac{1}{2}} \Delta x \frac{\delta_x^2 \theta_j}{\{2,4,6\}\delta_x \theta_{i+\frac{1}{2}}}. \tag{26}$$

For those schemes, the character of the diffusion depends on the ratio between the curvature at the upwind position $j = \{i \text{ if } u_{i+1/2} \geq 0; i+1 \text{ if } u_{i+1/2} < 0\}$ and the gradient at the edge. If the curvature and the gradient are of different sign, the diffusion coefficient becomes negative, which is not physical. Also, for the TVD (total variance diminishing) schemes G and I, it is not obvious whether the diffusion coefficient is always positive.

Figure 1 displays the weighted diffusion coefficient $K^{\theta}_{i+1/2} / (\mid u_{i+1/2} \mid \Delta x)$ for different schemes in dependence on r. Most of the schemes render negative diffusion coefficients locally possible even though they are sometimes designed to be TVD. The green curve for the superbee limiter has especially pronounced possibilities for negative coefficients. This coincides with the well-known observation that the superbee filter generates steps in smooth regions. This is a hint for antidiffusive behavior. Concluding, TVD schemes do not generally conform with the requirement of the second law of thermodynamics. Only the minmod limiter and the first order upwind scheme feature positive diffusion coefficients by design.

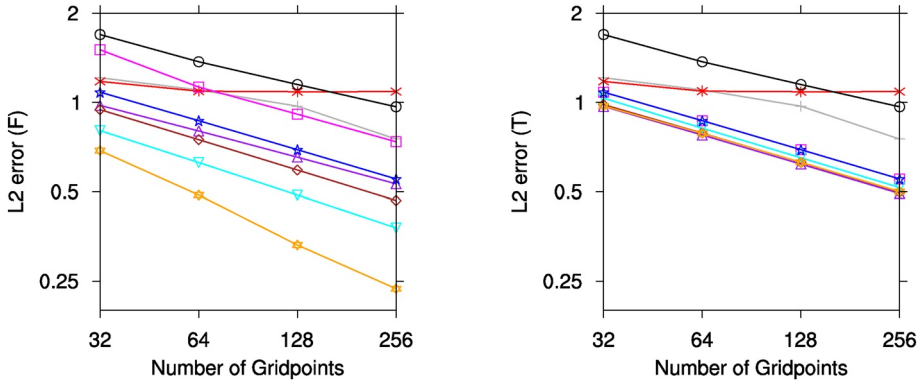

Figure 2. L2 errors for positivity switch false (F, left) and true (T, right). Gray crosses: no diffusion. Red asterisks: constant diffusion. Black circles: upwind. Magenta squares: Beam Warming. Purple upward pointing triangles: Fromm. Cyan downward pointing triangles: third order. Brown diamonds: van Leer. Blue pentagons: minmod. Orange hexagons: superbee.

From the above discussion about the physical necessity of positive internal entropy production, most of the mentioned diffusion coefficients have to be limited to positive values. Therefore, it is here suggested to correct them to match a proper physical appearance and write

$$K^{\theta,corr}_{i+1/2} = \max(0, K^{\theta}_{i+1/2}). \tag{27}$$

3.2. Test Case for Pure Advection

One of the typical test cases is the advection of a box function. For that testcase, the left and right halves of a periodic domain are initiated with function values 1 and 2, respectively. This function is advected analytically and numerically with a constant speed as long as that the analytic solution coincides with the initial condition. This means a revolution of the function once around the channel. The testcase is run with 32, 64, 128 and 256 points using a wind speed of $u = 0.5$ m/s and $\Delta x/\Delta t = 1$. A Runge Kutta third order scheme is taken for time integration and the nonadvective part is only added in the last substep of the Runge Kutta scheme. The constant diffusion scheme applies the coefficient $K^{\theta} = 0.05$ m^2/s. All test runs use the above schemes A–I in their original configuration and in a configuration which applies the correction (27). The correction runs must give the same results for the schemes A–C and H.

Figure 2 summarizes the measured L2 error norms. Only the original superbee limiter reaches a steeper slope with a decay rate of approximately 1.4. All other uncorrected schemes are the most only slightly better than first order accurate with a decay rate of approximately 1.25. The L2 error increases if the correction kicks into the schemes and the decay rates of all the schemes are close to 1.25. The constant diffusion scheme does not change the error for increasing resolutions after the first refinement. This signifies that for the fixed coefficient K^{θ} the "true" solution is achieved with a resolution of 64 gridpoints in this example. In physical space that would mean that DNS resolutions must have been reached. It has been verified (not shown here) that the character of the L2 error differences between the uncorrected and the corrected schemes is rather independent of the Courant number, as long as this number is smaller than 1. Even though a third order Runge Kutta scheme has been used here, larger Courant numbers are impossible, because the inherent damping properties are inherited from the TVD schemes.

Figure 3 displays the numerical solution to this problem for the coarsest resolution. It is striking that the additionally limited solutions avoid oscillations (except for the third order scheme) and make the solution to look more symmetric than the respective uncorrected counterparts. Figure 4 displays the numerical dissipation measure $\eta = K^{\theta}(\delta_x\theta \,/\, (\overline{\theta}\Delta x))^2$ adopted from Equation 18 under disregarding T, ϱ, and c_p for the coarsest resolution runs at the last time step. The dissipation should be always positive definite, but all uncorrected schemes feature locally negative dissipation rates at the leading edge of the jump.

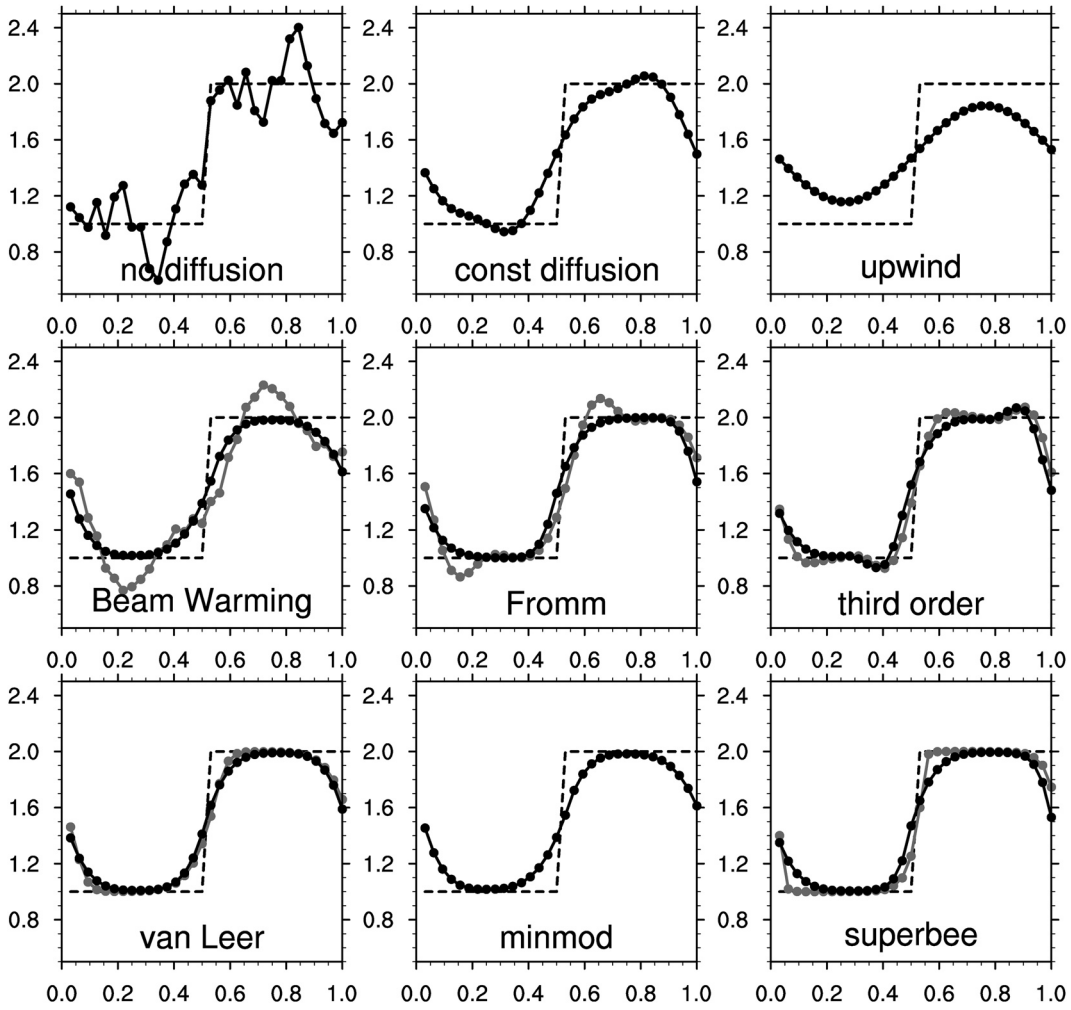

Figure 3. The solutions for the methods in the table for the lowest resolution run after one revolution. Dashed: analytic solution. Gray: original scheme. Black: positive K^{θ} corrected scheme.

A look onto the behavior in the spectral space is of interest, because numerical simulations of atmospheric flows are often judged for the ability to represent reasonable available potential (APE) or kinetic energy (KE) spectra (Malardel & Wedi, 2016; Skamarock, 2004). The panels of Figure 5 display the amplitude spectra of θ. When looking at such a spectrum in a full atmospheric model, it would represent the APE spectrum. Since the moving box problem is antisymmetric about the midst of the channel, only every second Fourier amplitude is significant. Only the uneven cos functions are initiated, because they are zero at $\pm\pi/2$. The uneven sin functions are initiated because they have opposing signs at $\pm\pi/2$. This feature is kept for all schemes, except the superbee scheme, which has significant amplitudes also for even wavenumbers that increase with increasing wave number index. Those amplitudes remain always smaller than the amplitudes for the uneven wave number indices. In the coarse resolution run, this effect is not yet visible. Interestingly, the scheme without diffusion (A) coincides the best with the analytic spectrum, especially for the coarse resolution run. But the fine resolution run indicates more clearly the problem of the no diffusion scheme. The amplitudes for the smallest wavelengths increase again so that the spectrum attains a hook. This is a sign of nondissipative behavior and accumulation of wave energy near the grid scale. Here, this is a result of the dispersion error of the centered difference scheme. All other schemes besides scheme A exhibit a fall off of the spectrum toward higher wavenumbers. This is even the case for the superbee scheme I which exhibits the smallest L2 error otherwise. Transferring this behavior to a full atmospheric model, it becomes

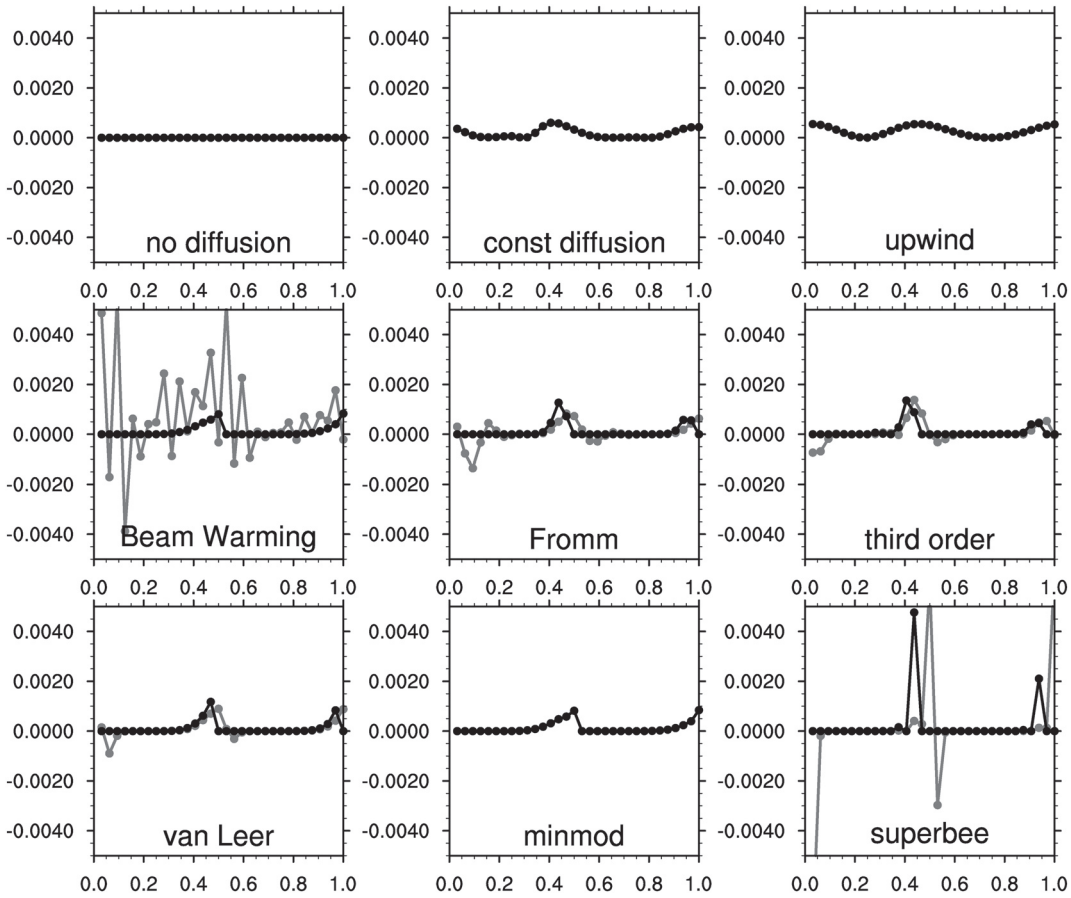

Figure 4. The dissipation rates $K^{\theta}(\partial_x \theta / \theta)^2$ for the methods in the table for the lowest resolution run after one revolution. Gray: original scheme. Black: positive K^{θ} corrected scheme.

clear that we must expect a fall off of the APE and KE spectra from the effective resolution scale toward the truncation scale (Skamarock, 2004). This insight should be kept in mind when judging full kinetic energy spectra or available potential energy spectra of any model.

The inspection of wave number spectra may be accompanied with a study of the phases of the wave modes. Selected phase spectra of the uneven wavenumbers are displayed in Figure 6. The uncorrected versions of schemes D–F and the not drawn results of schemes A–C feature chaotic phase behavior. However, the corrected versions have all a structured phase behavior. Here, the aim for modeling should be that the phases remain close to the analytic solution as long as possible. The van Leer scheme performs best in this regard. But also the corrected Fromm scheme and the minmod limiter approximate the phases relatively good. Their phase errors are of opposite sign. This spectral behavior is visible in the gridpoint space (Figure 3) as the opposing weighting of the black lines toward the head (Fromm) and toward the tail (minmod limiter) of the original box. For the van Leer limiter such a bulging is almost not visible by eye. The corrected superbee limiter does not perform well with regard to the phase properties.

The specific advection scheme for a full atmospheric model remains a matter of choice. But if we look at the error norms for the corrected runs, the differences among the schemes D–I are comparatively small. This means on the other hand that the success of the elaborated uncorrected schemes has its roots in negative dissipation, hence antidiffusive behavior. In the next section, we will inspect how such negative dissipation rates modify the overall behavior of the flow field.

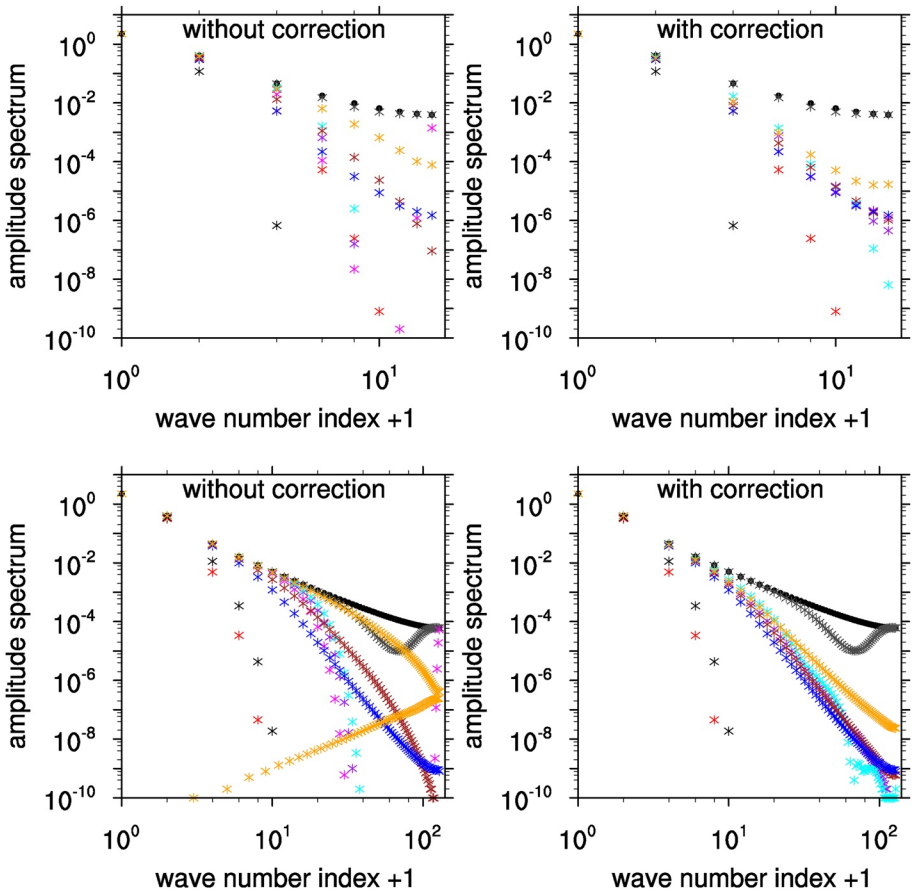

Figure 5. Amplitude spectra for the coarsest (upper panels) and finest (lower panels) resolution after one revolution. Black dots: analytic solution. Colored asterisks: Gray: no diffusion. Red: constant diffusion. Black: upwind. Magenta: Beam Warming. Purple: Fromm. Cyan: third order. Brown: van Leer. Blue: minmod. Orange: superbee.

4. Quasi-Adiabatic Simplified Dynamics

Now, the advection schemes of the previous section are used in the one-dimensional simplified dynamics equations with subgrid-scale terms of type 1 and 2. The combination of the two cases reads

$$\partial_t \varrho = -\partial_x(\varrho u) \tag{28}$$

$$\partial_t u = fv - \partial_x \frac{u^2}{2} - c_p \hat{\theta}\, \partial_x \Pi \tag{29}$$

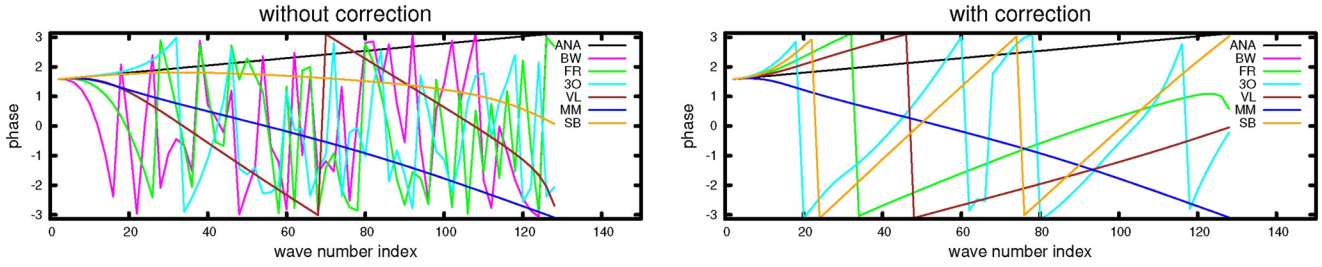

Figure 6. Phases for corrected and uncorrected runs. The analytic phases are given in black. Note that the solutions of the minmod limiter and the corrected Beam Warming scheme coincide.

$$\partial_t v = -u(\partial_x v + f) \tag{30}$$

$$\partial_t(\varrho\theta) = -\partial_x(\varrho u\hat{\theta}) - \frac{1}{c_p\Pi}\partial_x(-c_p\varrho K^T\partial_x T) \tag{31}$$

Here, $\hat{\theta} = \overline{\theta}_{i+1/2} - \frac{K^{\theta,corr}_{i+1/2}\delta_x\theta_{i+1/2}}{u_{i+1/2}\Delta x}$ and the $u_{i+1/2}$ in the denominator cancels with $|u_{i+1/2}|$ in the nominator, namely $K^{\theta,\mathrm{corr}}$, in amount. Hence, only the sign of it is inherited to $\hat{\theta}$. Momentum diffusion is omitted in the experiments. Intentionally, a simple representation of the Coriolis force is included.

The such defined simple dynamics model is now solved on a C-grid staggered mesh with constant mesh spacing. The kinetic energy is computed at unstaggered points $(u^2/2)|_i = (u^2_{i+1/2}/2 + u^2_{i-1/2}/2)/2$. All spatial differentials are represented by centered differences and the density is arithmetically averaged to the edge points. Then, an almost energy conserving implicit time discretization (Gassmann, 2013; Gassmann & Herzog, 2008) reads

$$u^{u+1} = u^n + \Delta t f v^{n+1} - \Delta t\partial_x\frac{u^{n+1}u^n}{2} - \Delta t c_p\hat{\theta}\partial_x\left(\frac{c_v}{c_p}\Pi^{n+1} + \frac{R}{c_p}\Pi^n\right) \tag{32}$$

$$\varrho^{n+1} = \varrho^n - \Delta t\partial_x\left(\frac{\varrho^n u^{n+1} + u^n\varrho^{n+1}}{2}\right) \tag{33}$$

$$\Pi^{n+1} = \Pi^n - \Delta t\frac{R\Pi^n}{c_v(\varrho\theta)^n}\partial_x\left(\frac{\varrho^n u^{n+1} + u^n\varrho^{n+1}}{2}\hat{\theta}\right) + \Delta t\frac{R}{c_v(\varrho\theta)^n c_p}\partial_x(c_p\varrho^n K^T\partial_x T). \tag{34}$$

Instead of prognosing $\varrho\theta$, the Exner pressure equation is integrated. It can be easily plugged into the pressure gradient term. This swapping of the prognostic variable is possible, because $\partial_t(\varrho\theta) = \frac{c_v\varrho\theta}{R\Pi}\partial_t\Pi$. The last term in Equation 34 is only significant in the constant diffusion case, where otherwise $\hat{\theta} = \overline{\theta}$. The values of $\hat{\theta}$ are obtained as for the pure advection runs from solving (19) with a RK3 scheme. Likewise, an RK3 scheme is used to put forward the meridional velocity equation to v^{n+1}. The problem to solve results in linear system $A \cdot x = b$, where $x = \{(\varrho^n u^{n+1} + u^n\varrho^{n+1})/2\}$ and A is a pentadiagonal matrix.

A test case is now designed with the aim of representing typical atmospheric conditions which would be encountered in a global atmospheric model, for instance for a front which develops in a baroclinic wave. Therefore, space and time dimensions are chosen to be $\Delta x = 30$ km and $\Delta t = 30$ s. The periodic model domain has $i_{\max} = 256$ gridpoints. In the experiments, the Coriolis parameter is either switched off or set to $f = 10^{-4}\mathrm{s}^{-1}$. The initial conditions are $u = 30$ m/s, $v = 0$ m/s, and $\theta = 280$ K in one half and 292 K in the other half of the periodic model domain. The Exner pressure is initiated with $\Pi = 1$. All other thermodynamic measures are deduced from those values via the equation of state. The comparison to a true three-dimensional model is still a bit problematic, because the adjustment process is accomplished here by acoustic speed, whereas in nature, this would be accomplished by the internal mode speed which is associated to a vertical structure function. This three-dimensionality cannot be projected into the one-dimensional simplified problem.

In case of the constant diffusion scheme, a coefficient of $K^T_{const} = 250000\, m^2/s$ is chosen. This is an unrealistic high value for air, but is used here as a means for magnifying how molecular diffusion would look like, if it would act on much larger scales. It has to be reminded here that the other inherently diffusive advection schemes have been developed for the use in dynamical contexts where steep gradients and discontinuities might occur, an analytic solution is not known and the resolution is too coarse to resolve molecular scales. Is has already been stressed toward the end of Section 2, that the inherent diffusion of those advection schemes is losing its dominating role if molecular diffusion is indeed acting and small scales are resolved.

The point to make here is that the second law of thermodynamics holds in any case, because the Gibbs fundamental relation distinguishes work and heat changes, where the heat changes describe all "macroscopically invisible" scales, hence all scales smaller than the grid scale, whereas the work can be determined until the smallest "macroscopically visible" scale, hence only for all scales larger than the grid scale.

Again, model runs are performed with all the above given numerical schemes A–I. For each experiment, two runs are performed. Either the corrected diffusion coefficient or the uncorrected diffusion coefficient is used. It is of interest how the dynamical measures like the winds, the divergence and pressure react to the different configurations.

Figure 7 displays the state of some selected variables after 2 h. Two main observations are striking. First, the no-diffusion run (A) does not feature any significant feedback on any dynamical variable. Second, the pressure will change, because the potential temperature or temperature is diffused/antidiffused, but the density is not modified. This is due to the relation $\varrho\theta = \frac{p_0}{R}\Pi^{c_v/R}$ or the relation $\varrho RT = p$. All dynamical effects must thus be interpreted as a reaction to the diffusion/antidiffusion alone because of this pressure change.

The effect of diffusion (not antidiffusion) at the jump when $\partial_x\theta > 0$ is now scrutinized. The pure diffusion case is realized in the constant diffusion run (scheme B), the upwind diffusion run (scheme C) and the minmod run (scheme H). θ increases/decreases to the left/right of the jump. Therefore, the pressure will change concurrently. This induces a pressure gradient such that the wind will be accelerated to the right, leading to positive u. These slight reactions can be interpreted as to prevent a further sideways dispersion of the box structure in θ. Thus, the θ field is expected to remain more coherent by dynamical support—not by reducing the diffusion of θ itself, which would have a similar effect. The pressure perturbations will also induce acoustic waves, which run away in both directions. This is reflected most impressively in the Exner pressure field. In contrast to the quickly propagating acoustic modes, the initial related wind perturbation and the associated divergence are persistent during the integration time. They are not fully converted into wave energy.

If the correction for the diffusion coefficient is not done and antidiffusion is allowed for, erroneous negative dissipation rates occur. This happens for all the other mentioned schemes D, E, F, G, and I. The corresponding velocity fields feature now locally opposite relative speeds compared to the previously discussed ones. Such negative wind perturbations would tend to destroy the coherent box structure, if coinciding with gradients of the scalar to be transported. In the present example, this coincidence does not happen for θ. Namely, the steepest gradients of θ are located to the left (grid points less than 200) of the negative wind perturbations (grid points larger than 200). But if there was a further tracer field, which does not interfere with the dynamics and has another spatial distribution, the advection of this field might become erroneously modified.

A striking feature of the various experiments is that the evolving pressure perturbations, and thus also the formation of acoustic waves, differ enormously among the experiments. Obviously, schemes exhibiting discontinuities in their diffusion coefficients excite much more of those waves. Such discontinuities are created by min, max operators. The increased level of pressure perturbations is independent of whether the max-operator serves only for the positivity of K^θ or is an inherent operator in the TVD schemes like minmod (H) or superbee (I). The minmod scheme delivers positive diffusion coefficients, but the θ-flux exhibits a jump, which is inherited to the wind perturbation and thus the divergence, where a true spike develops finally. This gives raise to large amplitudes in the acoustic modes in the pressure field. Similar discontinuous fluxes are created when limiting the original diffusion coefficients to positive values. Therefore, all the more entropically consistent schemes with $K^{\theta,\mathrm{corr}} = \max(0, K^\theta)$ exhibit this kind of larger amplitude pressure modes. Consequently, we expect also a higher level of gravity wave excitations near fronts if those schemes are used in full atmospheric models.

A further remark concerns the inclusion of the Coriolis force, which modifies the already described dynamics only slightly, see the lower two panels of Figure 7. The originally created zonal velocity perturbation is turned into a meridional component. This reduces the amplitude of the zonal velocity component and in turn also the amplitude of the divergence and the pressure perturbation. More energy is thus stored in the geostrophically balanced regime and less energy is available for the excitation of waves.

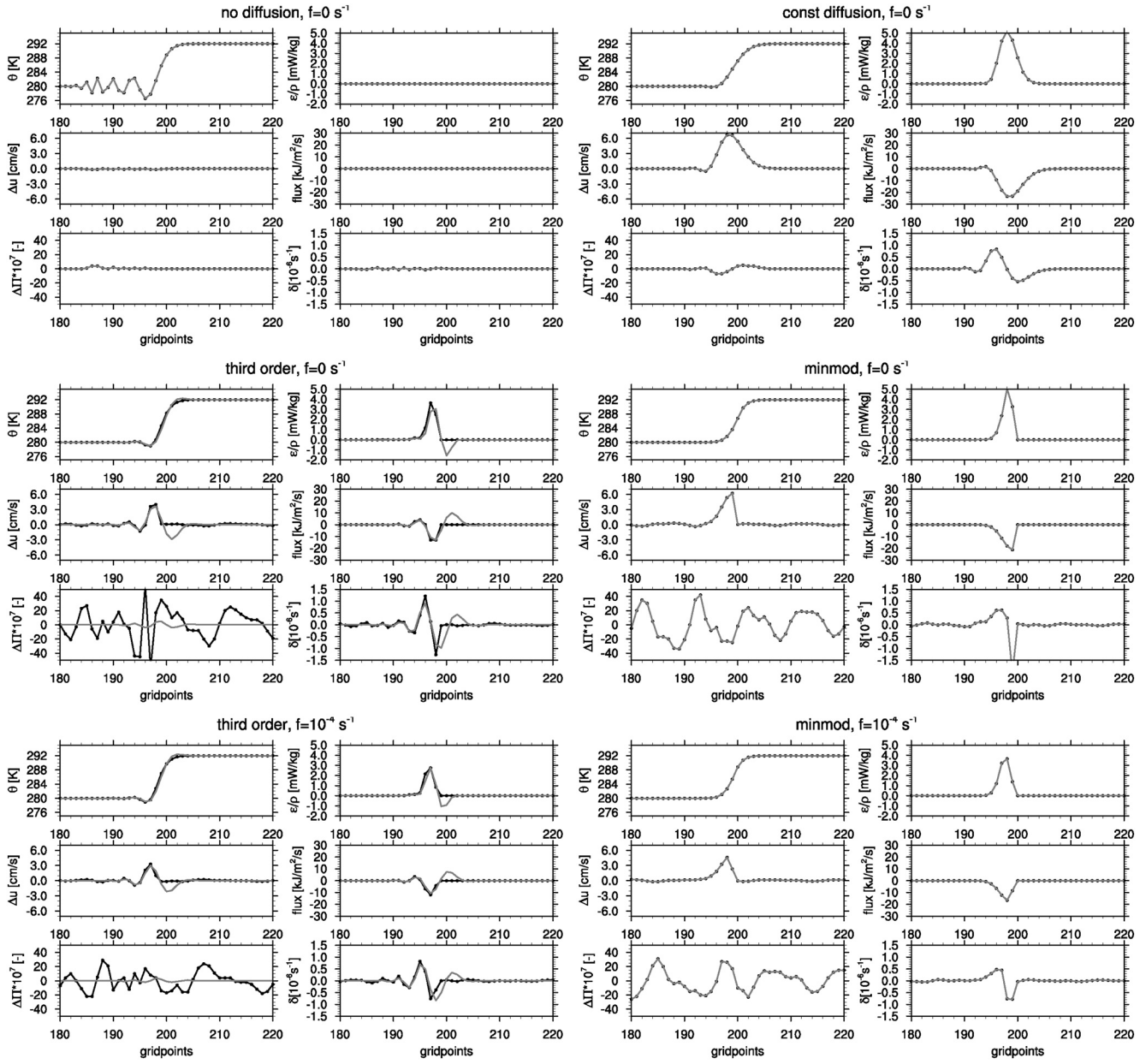

Figure 7. Results of selected variables near the jump for runs with advection schemes A, B, F and H for the one-dimensional dynamics testcase and $f = 0\ s^{-1}$ (upper four panels) and $f = 10^{-4} s^{-1}$ (lower two panels). Displayed variables are from upper left to lower right in each panel: potential temperature, specific dissipation, deviation of the wind from the actual mean, heat flux, deviation of the Exner pressure from the actual mean, and divergence. Black/gray lines show results of the run with/without corrected diffusion coefficients.

The given analysis demonstrates two opposing effects of the more entropically consistent approach compared to the original one. First, as a pro, the more physical plausible behavior of the induced velocity perturbation is appreciated. Second, as a con, undesired acoustic modes are created due to the more discontinuous character of the θ-fluxes themselves. A future investigation route could focus on the numerical treatment of too strong discontinuities in the fluxes, and thus aim at finding a means to reduce the level of undesired wave excitation.

It must be said here, that all the discussed perturbations are very small. Therefore, the effects onto simulations with a full atmospheric model are expected to remain small, too.

5. Dry Baroclinic Wave Test

In this section, a dry baroclinic wave test is performed with the ICON-IAP global nonhydrostatic model (Gassmann, 2013). This model uses a hexagonal C-grid for the dynamics. In the current configuration, the baroclinic wave initial conditions are taken from Gassmann (2019). Momentum is diffused via a horizontal Smagorinsky diffusion scheme, as formulated for the hexagonal C-grid in Gassmann (2018). This background diffusion is kept as small as possible by choosing a relatively small Smagorinsky parameter $c_s = 0.107$. The horizontal resolution is 30 km and 70 unequally spaced vertical levels up to 35 km height are used. Three runs are performed, a run with second order θ-advection, and two runs with the third order advection of Skamarock and Gassmann (2011) where the limiting for positive inherent diffusion coefficients is switched on or off, respectively. This third order scheme is an adaptation of scheme F for the hexagonal C-grid. Specifically, the Skamarock and Gassmann (2011) scheme determines an edge value $\hat{\theta}^e$ from two addends. One addend is the arithmetic average $\overline{\theta}^e$ obtained from the two adjacent cells, and the second addend, θ_d, is built upon normal-edge directional Laplacians of θ at the adjacent cell centers. The first addend drives the scheme second-order accurate and the addition of the second addend may lead to higher order accuracy, see Equation 7 of Skamarock and Gassmann (2011). In order to drive the second addend to conform with a downgradient flux form, this term is reformulated to

$$\theta_d = -\frac{\mathrm{sgn}(\partial_n\theta - J_n\partial_z\theta)}{\mathrm{sgn}(u_n)}\max\left[0, \frac{\mathrm{sgn}(u_n)}{\mathrm{sgn}(\partial_n\theta - J_n\partial_z\theta)}\frac{\Delta x^2}{6}(\partial_n^2\theta - J_n^2\partial_z\theta)\,|_{\mathrm{upstream}}\right] \tag{35}$$

in case of the third order original scheme. Here, n denotes the edge normal direction, the gradients are approximated by centered differences and the directional Lapacians are reconstructed. For reference, also the terrain-following correction terms are given using the slopes J_n and directional Laplacians J_n^2 of the height of the coordinate lines.

Gravity waves are excited from frontal areas of the baroclinic wave. The degree to which they are formed depends on the advection scheme. The second order advection scheme is not diffusive, but since it has too significant phase errors, the resulting θ-field is very noisy (cf. Figure 3). Figure 8 reveals that the gravity waves that appear in such a simulation are exaggerated compared to the runs with the more smooth third order advection.

What concerns the third order runs, unphysical negative dissipation rates due to θ-advection are to be found in the run with the original inherent diffusion (see Figure 9). The corrected scheme delivers only positive dissipation rates. The shape of the dissipation captures the front very precisely. Therefore, the dissipation could be used as a proxy for the frontogenesis function, which is often taken as a gravity wave source indicator (Charron & Manzini, 2002). However, the measured dissipation is rather a reaction to strong frontogenesis, which can no longer be resolved by the model. Remarkably, the frontogenesis function has been found by Kim et al. (2016) to fail as an indicator for gravity wave formation from jets and fronts in some cases. The dissipation function could possibly provide a better indicator.

The formation of gravity waves is differently modified by both third order runs. As discussed for the one-dimensional dynamics, the more discontinuities are present in the θ-fluxes, the more pressure perturbations are excited, and the more likely is the increase in gravity wave amplitude. This behavior is directly visible when comparing the near-front divergence amplitudes between the runs with limited and non-limited inherent diffusion coefficients of the advection schemes (Figure 8). Even though the limited diffusion coefficients deliver a more smooth θ-field, the level of gravity wave amplitude increases at least slightly. This is almost invisible at lower levels, but the difference between the runs comes to the fore at higher levels. In the plots it is best seen when comparing the wave structure about 50 N, 134 E. Such increased gravity wave amplitudes are in contrast to the previous finding by Plougonven and Snyder (2007), who found that the amount of dissipation (including frictional dissipation) is shaping the amplitude of the waves. Here, it is concluded that the specific shape and structure of the dissipation is likewise responsible for the extent to which gravity waves are numerically excited.

The limited diffusion coefficients lead to less accurate solutions and as a consequence, the speed of the overall baroclinic development is slowed down, see Figure 10. This has already been reported in Skamarock

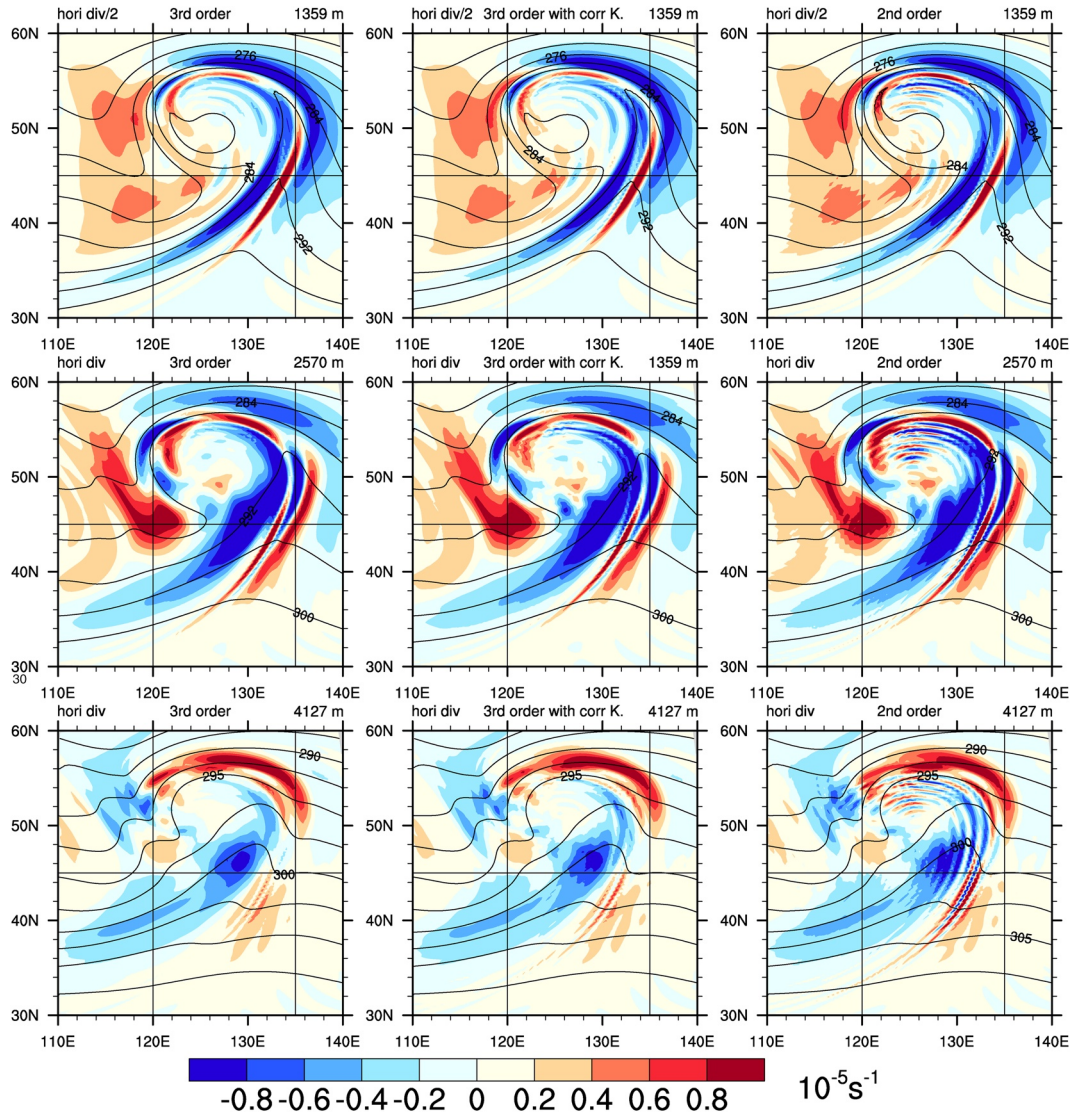

Figure 8. Horizontal divergence in s^{-1} (colors) for the original third order (left), entropically consistent third order (center), and the second order (right) θ-advection scheme at day 7 in about 1,359 m (upper row), 2,570 m (middle row), and 4,170 m (lower row) height. The values in the first row are divided by two in order to meet the same color scale. The contours display the potential temperature in Kelvin.

and Gassmann (2011), Figure 14. There, this effect was shown to lead to pronounced phase errors in coarse resolution runs with grid resolutions of 240 km. Here, the mesh is finer, namely 30 km, and therefore this effect is not as much pronounced, but still noticeable. Figure 10 reveals that both, the second order and the corrected third order runs, are lagged behind the original third order run, because the surface pressure is deeper downstream and higher upstream in comparison to the third order run. Furthermore, there is no phase lag between the second order and the corrected third order run, but the corrected third order run exhibits a less deep surface pressure in the center of the cyclone compared to the second order run. This is explicable when considering baroclinic development from the standpoint of quasi-geostrophic theory. There, temperature and vorticity depend on the evolution of one single variable, namely the geopotential. Therefore, if the temperature field becomes less accurate and more smooth due to the selected numerical scheme, the vorticity field inherits the same properties.

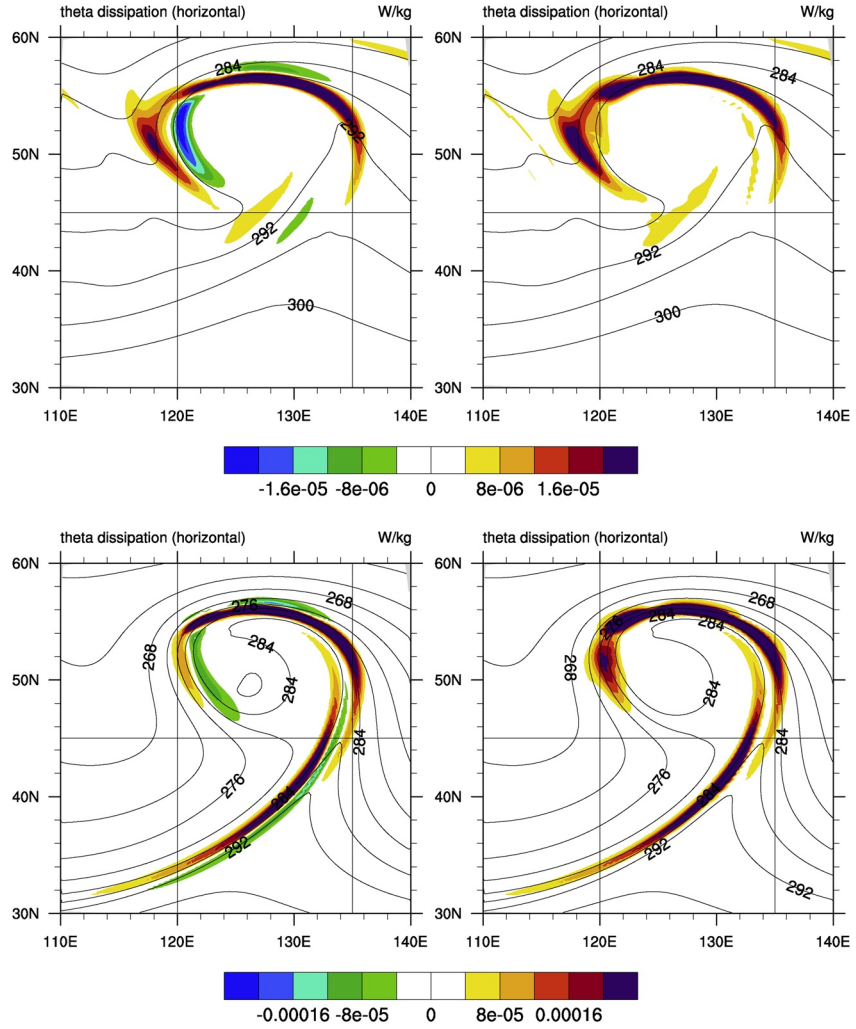

Figure 9. Dissipation rates (colors) for the original (left) and entropically consistent (right) θ-advection scheme at day 7 in about 2,500 (upper row) and 500 m (lower row). The contours display the potential temperature in Kelvin.

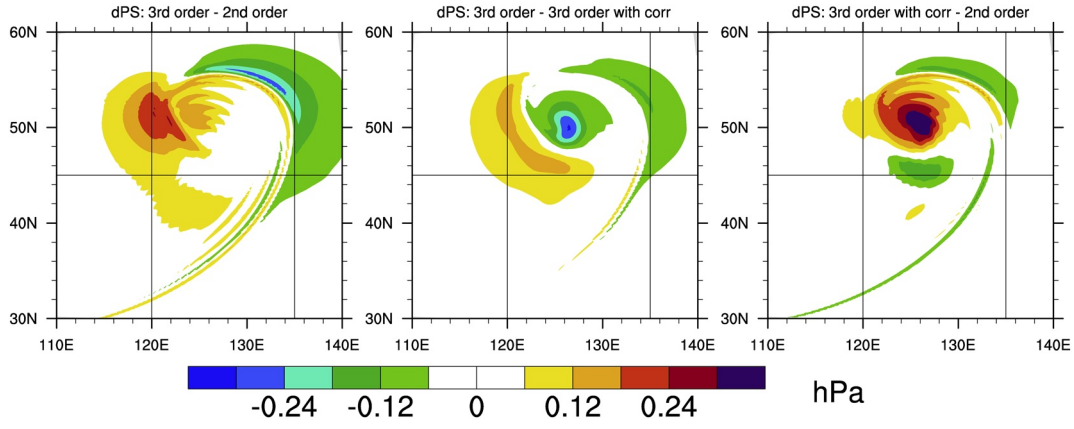

Figure 10. Surface pressure differences in hPa at day 7 between different runs, from left to right: third order minus second order, third order minus third order with correction, third order with correction minus second order.

6. Conclusion

This study discusses several aspects of inherently diffusive advection schemes for the potential temperature in atmospheric models. The main issues discussed were

1. The consistency with underlying physical laws: energy conservation and local entropy production
2. The accuracy
3. The amplitude of excited gravity waves from simulated fronts

It is clear that our model equations have to obey underlying physical laws like energy conservation and entropy increase. In this study, it has been demonstrated that the numerical accuracy is degraded when strictly following these rules. This is because higher order accurate numerical advection schemes necessarily involve antidiffusive fluxes. Those fluxes are unphysical and lead to local entropy destruction, and in turn an erroneous response of the full physical system. In our case, the antidiffusive fluxes lead to a wind acceleration into the wrong direction. When prohibiting such fluxes by replacing the negative diffusion coefficients with zero, the accuracy decreases, the physical consistency improves and a discontinuity in the fluxes is established so that higher amplitude gravity waves are excited from fronts.

There is a clear ambiguity in the results, because the actual goal, namely achieving high accuracy, consistency with underlying physical laws and a trustable level of gravity wave formation may not be reached in conjunction. For the first two points, accuracy and consistency, we have analytic means for assessments at hand, but for the third point, we do not have an independent analytic tool that tells us whether the amount of gravity wave formation in a model occurs for the right reason. This is because the physical scales of gravity waves are often comparable to the effective resolution scale. At this scale, the phase errors of the advection scheme come to the fore and the numerics is predominantly necessary to tackle these errors.

With regard to the excitation of gravity waves we learn that those waves are the more excited the more discontinuous the body force is in the momentum equation. In reality, such gravity waves exist due to several forcings, not only thermal diffusion, but also nonlinear advection and turbulent diffusion. The model captures their pattern quite well. Besides their pattern, the amplitude of these waves may not be precisely determined, because it depends too much on the numerical details.

One consequence from all those insights could be to increase the numerical accuracy of the whole equation set. That includes increasing the order of accuracy of the gradient, the divergence and rotation operators and retaining the energetically and entropically consistent framework at the same time.

Data Availability Statement

The data and source code which are relevant for this study are available from https://doi.org/10.22000/354

Acknowledgments
This study is a contribution to the project M4 (Entropy production in turbulence parameterizations) of the Collaborative Research Centre TRR 181 "Energy Transfer in Atmosphere and Ocean" funded by the Deutsche Forschungsgemeinschaft (DFG, German Research Foundation)—Projektnummer 274762653."

References

Bannon, P. R. (2002). Theoretical foundations for models of moist convection. *Journal of the Atmospheric Sciences*, *59*(12), 1967–1982. https://doi.org/10.1175/1520-0469(2002)059⟨1967:TFFMOM⟩2.0.CO;2

Catry, B., Geleyn, J.-F., Tudor, M., Bénard, P., & Trojáková, A. (2007). Flux-conservative thermodynamic equations in a mass-weighted framework. *Tellus A: Dynamic Meteorology and Oceanography*, *59*(1), 71–79. https://doi.org/10.1111/j.1600-0870.2006.00212.x

Charron, M., & Manzini, E. (2002). Gravity waves from fronts: Parameterization and middle atmosphere response in a general circulation model. *Journal of the Atmospheric Sciences*, *59*(5), 923–941. https://doi.org/10.1175/1520-0469(2002)059⟨0923:GWFFPA⟩2.0.CO;2

Degrauwe, D., Seity, Y., Bouyssel, F., & Termonia, P. (2016). Generalization and application of the flux-conservative thermodynamic equations in the AROME model of the ALADIN system. *Geoscientific Model Development*, *9*(6), 2129–2142. https://doi.org/10.5194/gmd-9-2129-2016

de Groot, S. R., & Mazur, P. (1984). *Nonequilibrium thermodynamics*. Dover.

Dubos, T., & Tort, M. (2014). Equations of atmospheric motion in non-eulerian vertical coordinates: Vector-invariant form and quasi-Hamiltonian formulation. *Monthly Weather Review*, *142*(10), 3860–3880. https://doi.org/10.1175/MWR-D-14-00069.1

Durran, D. (2010). *Numerical methods for fluid dynamics: With applications to geophysics*. New York, NY: Springer. https://doi.org/10.1007/978-1-4419-6412-0

Eldred, C., & Gay-Balmaz, F. (2020). Single and double generator bracket formulations of multicomponent fluids with irreversible processes. *Journal of Physics A: Mathematical and Theoretical*, *53*(39), 395701. https://doi.org/10.1088/1751-8121/ab91d3

Gassmann, A. (2013). A global hexagonal C-grid non-hydrostatic dynamical core (ICON-IAP) designed for energetic consistency. *Quarterly Journal of the Royal Meteorological Society*, *139*, 152–175. https://doi.org/10.1002/qj.1960

Gassmann, A. (2018). Discretization of generalized Coriolis and friction terms on the deformed hexagonal c-grid. *Quarterly Journal of the Royal Meteorological Society*, *144*(716), 2038–2053. https://doi.org/10.1002/qj.3294

Gassmann, A. (2019). Analysis of large-scale dynamics and gravity waves under shedding of inactive flow components. *Monthly Weather Review*, *147*(8), 2861–2876. https://doi.org/10.1175/MWR-D-18-0349.1

Gassmann, A., & Herzog, H.-J. (2008). Towards a consistent numerical compressible non-hydrostatic model using generalized Hamiltonian tools. *Quarterly Journal of the Royal Meteorological Society*, *134*(635), 1597–1613. https://doi.org/10.1002/qj.297

Gassmann, A., & Herzog, H.-J. (2015). How is local material entropy production represented in a numerical model? *Quarterly Journal of the Royal Meteorological Society*, *141*, 854–869. https://doi.org/10.1002/qj.2404

Kim, Y.-H., Chun, H.-Y., Park, S.-H., Song, I.-S., & Choi, H.-J. (2016). Characteristics of gravity waves generated in the jet-front system in a baroclinic instability simulation. *Atmospheric Chemistry and Physics*, *16*(8), 4799–4815. https://doi.org/10.5194/acp-16-4799-2016

Malardel, S., & Wedi, N. P. (2016). How does subgrid-scale parametrization influence nonlinear spectral energy fluxes in global NWP models? *Journal of Geophysical Research: Atmospheres*, *121*(10), 5395–5410. https://doi.org/10.1002/2015JD023970

Névir, P., & Sommer, M. (2009). Energy–vorticity theory of ideal fluid mechanics. *Journal of the Atmospheric Sciences*, *66*(7), 2073–2084. https://doi.org/10.1175/2008JAS2897.1

O'Sullivan, D., & Dunkerton, T. J. (1995). Generation of inertia–gravity waves in a simulated life cycle of baroclinic instability. *Journal of the Atmospheric Sciences*, *52*(21), 3695–3716. https://doi.org/10.1175/1520-0469(1995)052⟨3695:GOIWIA⟩2.0.CO;2

Plougonven, R., & Snyder, C. (2007). Inertia-gravity waves spontaneously generated by jets and fronts. Part I: Different baroclinic life cycles. *Journal of the Atmospheric Sciences*, *64*(7), 2502–2520. https://doi.org/10.1175/JAS3953.1

Plougonven, R., & Zhang, F. (2014). Internal gravity waves from atmospheric jets and fronts. *Reviews of Geophysics*, *52*(1), 33–76. https://doi.org/10.1002/2012RG000419

Schoon, L., & Zülicke, C. (2018). A novel method for the extraction of local gravity wave parameters from gridded three-dimensional data: Description, validation, and application. *Atmospheric Chemistry and Physics*, *18*(9), 6971–6983. https://doi.org/10.5194/acp-18-6971-2018

Skamarock, W. C. (2004). Evaluating mesoscale NWP models using kinetic energy spectra. *Monthly Weather Review*, *132*(12), 3019–3032. https://doi.org/10.1175/MWR2830.1

Skamarock, W. C., & Gassmann, A. (2011). Conservative transport schemes for spherical geodesic grids: High-order flux operators for ODE-based time integration. *Monthly Weather Review*, *139*, 2962–2975. https://doi.org/10.1175/MWR-D-10-05056.1